

PLASMA FLOW CONTROL FOR NOISE REDUCTION
ON A G550 NOSE LANDING GEAR:
THE DEVELOPMENT OF A PLASMA FAIRING

A Prospectus for a Dissertation

Submitted to the Graduate School
of the University of Notre Dame
in Partial Fulfillment of the Requirements
for the Degree of

Doctor of Philosophy

by
Michael C. Wicks

Flint O. Thomas, Director

Graduate Program in Aerospace and Mechanical Engineering

Notre Dame, Indiana

December 2015

© Copyright by
Michael C. Wicks
2015
All Rights Reserved

CONTENTS

FIGURES	iv
TABLES	v
CHAPTER 1: INTRODUCTION	1
1.1 Motivation	3
1.2 Theory of Aeroacoustics	3
1.3 Landing Gear	7
1.3.1 Geometry	8
1.3.2 Noise Sources	8
1.4 Literature Review	12
1.4.1 Single Cylinder Plasma Flow Control	12
1.4.2 Tandem Cylinders Plasma Flow Control	13
1.4.3 Shock Strut-Torque Arm Assembly Plasma Flow Control	14
CHAPTER 2: EXPERIMENTAL APPROACH	17
2.1 Experimental Objective	17
2.2 Experimental Facility	17
2.3 Notre Dame G550 Nose Landing Gear Model	19
2.4 Microphone Measurements	19
2.5 Flow Visualization	20
2.6 Data Acquisition	21
2.7 Current Results	23
2.7.1 Wind Tunnel Background Noise Characterization	23
2.7.2 Far field check	23
2.7.3 Comparison with UFAFF Measurements	25
2.7.4 Effects of Tripping	28
2.7.5 Preliminary Acoustic Assesment	28
CHAPTER 3: OBJECTIVES AND FUTURE WORK	35
3.1 Research Objectives	35
3.2 Proposed Future Work	35
3.2.1 Plasma Actuator Configuration	36
3.2.2 Noise Reduction Assessment	36
3.3 Conclusion	37

BIBLIOGRAPHY	38
------------------------	----

FIGURES

1.1	Photograph of Gulfstream 550 Nose Landing Gear.	8
1.2	Schematic view of Gulfstream 550 Nose Landing Gear components [9].	9
1.3	Flow Visualization of single cylinder in cross-flow with Spanwise and PSVG plasma actuators.	13
1.4	Flow Visualization of tandem cylinders in cross-flow with Spanwise and PSVG plasma actuators.	15
1.5	Flow Visualization of torque-arm assembly in cross-flow with Spanwise plasma actuators.	16
2.1	ND G550 model with and without plasma fairing installed.	18
2.2	Schematic of the polar array.	20
2.3	Photograph of the polar array installed in the ND AWT.	21
2.4	Photograph of the experimental setup for high speed flow visualization.	22
2.5	Representative far field noise level with and without Baseline 1 model installed at $\theta = 90^\circ$	24
2.6	Far field measurement analysis for $d = 48$ in and $d = 59$ in at $\theta = 90^\circ$	25
2.7	Comparison of far field noise level at UFAFF and ND AWT facilities at $\theta = 90^\circ$	27
2.8	Comparison of design of the NASA G550 and ND G550 model geometries.	27
2.9	Comparison of far field noise level with and without the presence of a trip at $\theta = 90^\circ$	29
2.10	1/3-octave band sound pressure level for various plasma actuator configurations.	32
2.11	Overall sound pressure level at key polar array locations.	33
2.12	Landing gear flow visualization orthogonal (left) and at 45° (right). .	34

TABLES

1.1	Physical mechanisms of flow-generated noise.	12
2.1	Data acquisition parameters.	22

CHAPTER 1

INTRODUCTION

Air travel in the U.S. is steadily growing due in part to an improving economy. Landings and take-offs at airports with FAA-operated towers and FAA-contracted towers are forecasted to increase from 48.9M to 59.9M or 22.5% between 2015 and 2035 [20]. With the continuing growth of air traffic, additional airports are being built and existing airports are expanding. As this occurs, it is hard to ignore a significant byproduct: the increase in noise caused by aircraft.

The steady encroachment of airports is especially problematic in metropolitan areas, where aircraft noise can negatively impact quality of life. While this issue began as a public interest initiative, a recent study has found a statistically significant link between aircraft noise and cardiovascular disease [2]. Correia et al. looked at 89 of the largest airports across the U.S., and found that, even when controlling for other environmental factors, a 10 dB increase in noise was associated with a 3.5 % increase in hospital admissions in patients 65 years and older. Additional studies are ongoing, especially in the UK and EU, examining other potential adverse health effects such as delayed cognitive development in children [7]. In light of these studies, it is clear: engineers and scientists have an ethical imperative to ensure the safety of technology.

Progress is being made in the field of aeroacoustics. In general, aircraft have become “quieter”, especially due to the widespread adoption of the turbofan jet engine. With the reduction of jet engine noise, aircraft noise has come to a level comparable to that of the airframe on approach and landing conditions [4]. The airframe is the

new “lower noise barrier” of aircraft noise production. Efforts have been taken to quantify airframe noise. In a study by Gibson, flyover noise measurements were performed identifying landing gears and high-lift devices as the two major contributors to airframe noise [8].

In addition to these efforts, several government initiatives have been launched to advance quiet aircraft technology. In the EU, European Visions 2020 called for a reduction of “subjective noise impact by half” (minus 10 dB) per operation by 2020 relative to year 2000 level technology [1]. While in the US, the national Advanced Subsonic Transport (AST) and Quiet Aircraft Technology research programs have even more stringent milestones.

Due in part to these initiatives, several noise reduction technologies have been applied to aircraft landing gear. Dobrzynski et al. studied the effect of solid, streamlined add-on fairings to various areas of main and nose landing gears [5]. While these fairings were effective at reducing mid and high frequency noise levels, they had the drawback of increasing noise in the low frequency range. This study and those like it revealed that solid fairings acted to increase local flow velocity and thus noise from adjacent gear components.

The findings of work with solid fairing suggested the possibility that a porous fairing could streamline geometry while preventing the increase of local flow velocity. Ravetta et al. demonstrated the effects of elastic membrane fairings on reducing sideline noise for a 26%-scale Boeing 777 main landing gear [21]. They observed an average of 2 dB decrease over all frequencies and a 5 dB peak decrease at high-frequency (> 10 kHz). This was achieved through the application of fairings to main strut and brace locations. An elastic-membrane lower truck fairing was also examined yielding similar results.

These technologies share a common approach in that they each utilize passive flow control. The present work is focused on the use of active flow control via di-

electric barrier discharge (DBD) plasma actuation. Applications of this technology on geometries relevant to aircraft landing gear, suggest a potential advantage in this approach due to the variety of possible actuation strategies available. Examples are presented in the literature review section.

1.1 Motivation

The present work is motivated to reduce noise produced by aircraft landing gear by flow control via application of DBD plasma actuators. To this end, experiments will be performed to 1) better understand the noise generation mechanisms present on aircraft landing gear, thereby aiding in the formation of flow control strategies, and 2) take steps toward the development of “plasma fairing” technology, which is a device that can be retrofitted to existing aircraft landing gears with the purpose of reducing noise production.

In this chapter, the physics of airframe noise production is discussed. The structure of Aircraft landing gear is presented. This geometry is overviewed. Areas of noise contribution are considered and the underlying physical mechanisms are identified. Finally, the literature is reviewed with respect to the application of plasma flow control to increasingly complex geometries pertaining to aircraft landing gear.

1.2 Theory of Aeroacoustics

To arrive at a viable flow control strategy, it is useful to first review the underlying physics. The modern theory of aeroacoustics, that is sound generated by aerodynamic means, is based on James Lighthill’s so-called acoustic analogy. He states that sound generated in a fluid flow is only important in regions of turbulent fluctuations [12]. Based on this assumption, the Navier-Stokes Equation and isentropic equation of state in indicial notation are

$$\frac{\partial \rho}{\partial t} + \frac{\partial(\rho u_i)}{\partial x_i} = 0, \quad (1.1)$$

$$\frac{\partial(\rho u_i)}{\partial t} + \frac{\partial(\rho u_i u_j + P_{ij})}{\partial x_j} = 0, \quad (1.2)$$

$$c_o^2 = \frac{\partial p}{\partial \rho}|_{s=const.} = \frac{p'}{\rho'} \quad (1.3)$$

where

$$P_{ij} = p' \delta_{ij} - \sigma_{ij}. \quad (1.4)$$

P_{ij} is the total stress tensor, ρ is the fluid density, u is the local velocity vector, p is the pressure and c_o is the local speed of sound. Also, $p' = p - p_o$ and $\rho' = \rho - \rho_o$ represent the fluctuating pressure and density relative to the mean values, respectively. After assuming sufficiently small fluctuations, equations 1.1 and 1.2 can be linearized yielding the classical Lighthill's equation

$$\frac{\partial^2 \rho}{\partial t^2} - c_o^2 \nabla^2 \rho = \frac{\partial^2 T_{ij}}{\partial x_i \partial x_j}, \quad (1.5)$$

where the source term T_{ij} is known as Lighthill's turbulence stress tensor

$$T_{ij} = \rho u_i u_j + P_{ij} - c_o^2 (\rho - \rho_0) \delta_{ij}, \quad (1.6)$$

and where δ_{ij} is the Kronecker delta which is defined as,

$$\delta_{ij} = \begin{cases} 1 & \text{if } i = j \\ 0 & \text{if } i \neq j \end{cases}. \quad (1.7)$$

For the special case of high Reynolds number, incompressible flow, both the den-

sity fluctuations and the viscous stresses are negligible, reducing the Lighthill stress tensor to

$$T_{ij} \approx \rho_0 u_i u_j. \quad (1.8)$$

Equation 1.5 can be solved and formulated in terms of p' by combining with equation 1.3 giving

$$p' = c_o^2 \rho' = \frac{1}{4\pi} \frac{\partial^2}{\partial x_i \partial x_j} \int_V \frac{T_{ij}}{r} dV, \quad (1.9)$$

where V represents the volume of the region of interest, and r represents the distance to the acoustic source.

In 1955, Lighthill's analogy was extended to account for the presence of solid boundaries within the turbulent flow region [3]. The general solution to this equation is

$$\begin{aligned} p' = & \underbrace{\frac{1}{4\pi} \frac{\partial^2}{\partial x_i \partial x_j} \int_V \left[\frac{T_{ij}}{r} \right] dV}_I - \underbrace{\frac{1}{4\pi} \frac{\partial}{\partial x_j} \int_S \left[\frac{P_{ij} + \rho u_i u_j}{r} \right] n_i dS}_{II} \\ & + \underbrace{\frac{1}{4\pi} \frac{\partial}{\partial t} \int_S \left[\frac{\rho u_i}{r} \right] n_i dS}_{III}, \end{aligned} \quad (1.10)$$

where S represents the control surface bounding the volumetric region of interest [11]. Equation 1.10 forms the basis of airframe noise generation by including the effects of reflection and diffraction of acoustic waves at the boundaries.

To illustrate the nature of the acoustic source terms on the right hand side of equation 1.10, an order-of-magnitude scaling analysis is performed with the purpose of determining the radiation patterns of the hypothetical acoustic source with respect to flow speed, U_o , and propagation distance, r . Lighthill conveniently used a subsonic, turbulent isothermal jet to provide a physical application for which characteristic

length, frequency, pressure scales, and velocity can be defined [18]. Substituting the pertinent characteristic scales yields the following order-of-magnitude approximations for the components of the acoustic source term:

$$\int_V dV \propto D^3 \quad (1.11)$$

$$T_{ij} \propto \rho_o U_o^2 \quad (1.12)$$

$$\frac{\partial}{\partial x_i} = \frac{\partial}{c_o \partial t} \propto \frac{f}{c_o} \propto \frac{U_o}{c_o D} \quad (1.13)$$

Equations 1.11 - 1.13 are then utilized to replace the source terms in equation 1.10, resulting in the following:

$$I : \frac{1}{4\pi} \frac{\partial^2}{\partial x_i \partial x_j} \int_V \left[\frac{T_{ij}}{r} \right] dV \propto \left(\frac{U_o}{c_o D} \right)^2 (D^3) \left(\frac{\rho_o U_o^2}{r} \right) \propto \frac{U_o^4}{r}, \quad (1.14)$$

$$II : \frac{1}{4\pi} \frac{\partial}{\partial x_j} \int_S \left[\frac{P_{ij} + \rho u_i u_j}{r} \right] n_i dS \propto \left(\frac{U_o}{c_o D} \right) \left(\frac{\rho_o U_o^2}{r} \right) (D^2) \propto \frac{U_o^3}{r}, \quad (1.15)$$

$$III : \frac{1}{4\pi} \frac{\partial}{\partial t} \int_S \left[\frac{\rho u_i}{r} \right] n_i dS \propto \left(\frac{U_o}{D} \right) \left(\frac{\rho_o U_o}{r} \right) (D^2) \propto \frac{U_o^2}{r}. \quad (1.16)$$

This analysis assumes that the freestream Mach number is much less than unity or $M = \frac{U_o}{c_o} \ll 1$, and that far-field acoustic radiation dominates the signal so that it acts as a spherically-spreading pressure wave.

Furthermore, the radiated acoustic power W , is proportional to the square of the pressure field, giving

$$I : W \propto p'^2 \propto \frac{U_o^8}{r^2}, \quad (1.17)$$

$$II : W \propto p'^2 \propto \frac{U_o^6}{r^2}, \quad (1.18)$$

$$III : W \propto p'^2 \propto \frac{U_o^4}{r^2}. \quad (1.19)$$

The results of the scaling analysis presented in equation 1.17 correspond physically to the radiation pattern of a volumetric distribution of quadrupole sources. Therefore, Lighthill's acoustic analogy states that the far-field acoustic pressure field of a region of turbulence in a steady flow, and a region of quadrupole acoustic sources with no flow are equivalent. Similarly, equations 1.18 and 1.19 represent a distribution of dipole and monopole sources, respectively. Finally, this analysis shows that a decrease in acoustic power of the system corresponds to an increase in acoustic efficiency when transitioning from a quadrupole to a dipole to a monopole source. These trends are extremely useful in determining the nature of the acoustic sources present in flows around complex geometries, such as aircraft landing gears.

1.3 Landing Gear

As previously stated, aircraft landing gear have been identified as a primary source of airframe noise especially for the larger wide-body configurations. Landing gear generally come in two types: nose landing gear (NLG) and main landing gear (MLG). The former is designed for steering while the latter is designed for braking. The scope of this study is limited to work on the G550 nose landing gear, but while designs are aircraft-specific, it is probable that flow control strategies will be derived from general flow behavior, and therefore be universally applicable.



Figure 1.1. Photograph of Gulfstream 550 Nose Landing Gear.

1.3.1 Geometry

The Gulfstream G550 Nose landing gear was selected due to an industry collaboration with NASA. In Neuhart et al., this design was aerodynamically characterized to provide a database of aerodynamic and acoustic data by which to compare experiments and simulations [19]. The actual landing gear is depicted in Figure 1.1 for reference, and shown schematically in Figure 1.2.

1.3.2 Noise Sources

Recall that adding a solid boundary to the flow drastically altered the source terms in equation 1.10. In experiments, these terms manifest as flow-generated noise, of which there are two types: 1) Tonal which is generated by periodic flow events, such as vortex shedding, and 2) Broadband which is generated by random flow events, like

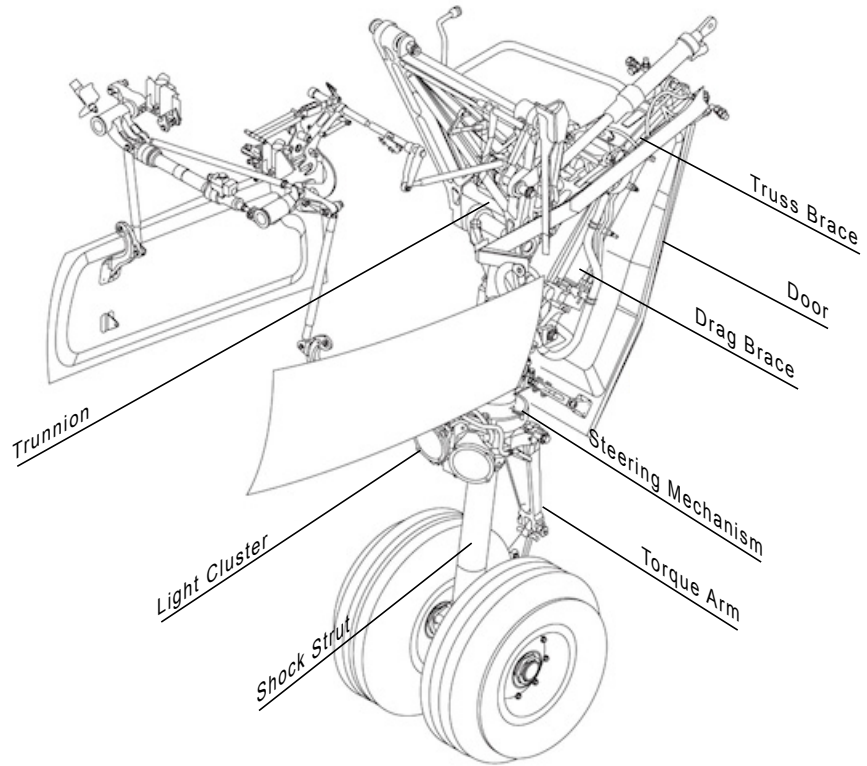


Figure 1.2. Schematic view of Gulfstream 550 Nose Landing Gear components [9].

those present in turbulence.

To develop technology to control these flow events, it is useful to understand the structures that cause them. Most aerodynamic bodies are characterized by their drag force, where the total drag force is made up of viscous drag and pressure drag components. When a body is streamlined, it is said that the total drag force is dominated by the viscous forces; while bodies characterized by a large pressure drag force, are referred to as bluff. Bluff bodies can be a major contributor to flow-generated noise, due in part to the unsteady wake these structures tend to cause.

The canonical example of a bluff body is a simple cylinder, for which the flow is well understood. It is dominated by large-scale vortex shedding of frequency f , over the cylinder body of characteristic length L . This vortex shedding frequency is characterized by the dimensionless Strouhal number $St = \frac{fL}{U_o}$ where U_o is the freestream velocity. This large-scale vortex shedding corresponds to periodic unsteady surface pressure which is responsible for the generation of tonal noise.

More complex geometries such as aircraft landing gear, can be considered as a collections of bluff bodies. As depicted in Figure 1.1, the landing gear components are arranged in close proximity to one another. However unlike the single cylinder, tonal behavior is not observed. The acoustic signature for the landing gear is broad-band in nature which is associated with turbulence [23].It is possible that the close proximity of gear components inhibits full wake development, effectively preventing the development of large-scale vortex shedding. This suggests that flow control on simplified geometries, while academically interesting, may not be representative of the flow physics present in actual aircraft structures. This is the foundation for the suggested strategy of examining sub-systems, proposed in Chapter 3.

In addition to varying inter-component spacings, the presence of multiple length scales in the landing gear geometry implies that some components may also contribute to the total noise as reflective sources. Guo et al., measured far-field noise

propagation for full-scale Boeing 737 main landing gear and classified it into regimes based on the concept of acoustic compactness [10]. Since an acoustic wave in a medium is governed by the speed of sound then $c_o = \lambda f$, a source is said to be acoustically compact if $kL \ll 1$ where k is the acoustic wavenumber defined as $k = \frac{2\pi}{\lambda} = \frac{2\pi f}{c_o}$, λ is the acoustic wavelength, and L is the characteristic length. It is noncompact if $kL \geq 1$. In Guo et al., large (wheels and doors) and medium geometries (main struts and linkages) represented low and mid-range frequency, acoustically compact sources, respectively; while small geometries (hoses, sharp edges, and electrical wiring) represented high frequency, noncompact acoustic sources. This is significant because compact sources behave like a distribution of dipoles, whereas noncompact sources tend to emit as, less efficient, quadrupoles.

Before discussing a strategy for flow control, it is useful to first consider the physical phenomena present. While quantifying the contribution of each mechanism to the total acoustic signature of the landing gear, is a fairly difficult task, an order-of-magnitude analysis can be applied to estimate a potential dominant source. Table 1.1 lists the mechanisms considered, acoustic power, noise type, and source type. Recall that high acoustic power corresponds to low acoustic efficiency, meaning a monopole source is a more effective noise producer than a quadrupole source. Focusing on the more efficient dipole sources present, the mechanisms of unsteady wake and downstream wake impingement are the most viable candidates for flow control. Note that vortex shedding may be present but is highly tonal, and the broadband nature of landing gear noise suggests that this is probably a minor noise producer. These physical phenomena are considered in the following review of literature.

TABLE 1.1

Physical mechanisms of flow-generated noise.

Mechanism	Acoustic Power	Source Type	Noise Type
Vortex Shedding	$\frac{U_o^6}{r^2}$	Dipole	Tonal
Wake Shear Layer	$\frac{U_o^8}{r^2}$	Quadrupole	Broadband
Wake Turbulence	$\frac{U_o^8}{r^2}$	Quadrupole	Broadband
Downstream Wake Impingement	$\frac{U_o^6}{r^2}$	Dipole	Broadband
Unsteady Wake	$\frac{U_o^6}{r^2}$	Dipole	Broadband
Reflective Sources	$\frac{U_o^8}{r^2}$	Quadrupole	Tonal or Broadband

1.4 Literature Review

This section provides a review of aeroacoustic research pertinent to the development of the aforementioned plasma fairing technology.

1.4.1 Single Cylinder Plasma Flow Control

The single cylinder is the most simplified representation of the landing gear main strut. Active flow control efforts by means of DBD plasma actuators were first applied to this generic bluff body geometry as proof-of-concept. Several experiments and large-eddy simulations (LES) were performed at the University of Notre Dame to show the viability of this technology [15] [16]. Two flow control technologies were employed: spanwise plasma actuators, and plasma streamwise vortex generators (PSVGs). The former of these devices consists of spanwise-oriented, exposed electrodes fixed about the geometry's separation points, while the latter is made up of a spanwise array of electrodes oriented in the streamwise direction. The construction and accompanying electronic circuit of these actuators are well documented in

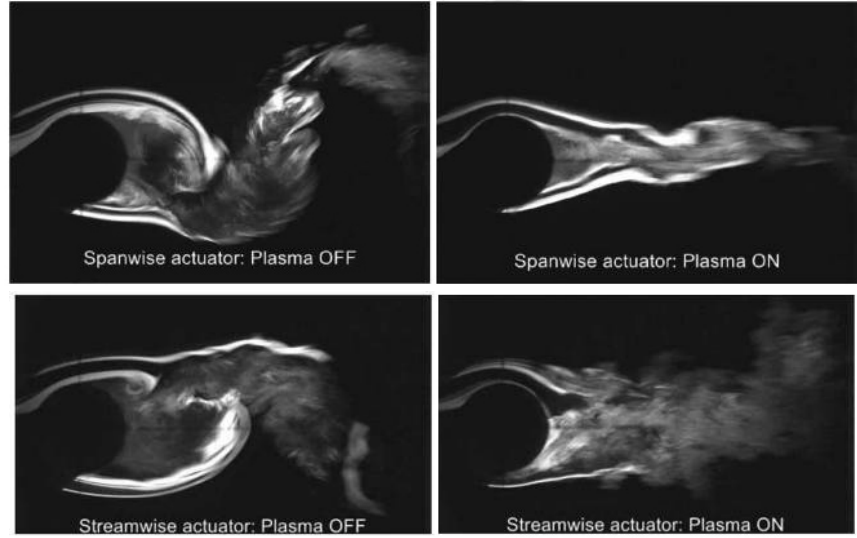


Figure 1.3. Flow Visualization of single cylinder in cross-flow with Spanwise and PSVG plasma actuators.

Kozlov et al. [16]. Flow visualization demonstrating the effects of these devices is shown in Figure 2.12.

Both approaches were effective in significantly suppressing large-scale vortex shedding, if by different mechanisms. Spanwise plasma actuators achieve flow control through modification of the detached free shear layer. PSVGs induce streamwise vorticity into the nascent cylinder wake, promoting rapid wake mixing. Kozlov et al. performed near field microphone measurements at $d = 0.61$ m, demonstrating a reduction in noise levels of 11.2 dB and 14.2 dB for spanwise actuators and PSVGs, respectively [16]. These results were promising and inspired more studies on a slightly more complex geometry: tandem cylinders.

1.4.2 Tandem Cylinders Plasma Flow Control

The tandem cylinders configuration is the next stage in the development of active plasma flow control for aircraft landing gear. Similar to the work on the single cylinder, experiments and LES were also performed for tandem cylinders as reported

in [6] [14] [17]. The interaction between the two bluff bodies represents that between the main strut and downstream components of an aircraft landing gear. In 1985, Zdravkovich comprehensively reviewed two circular cylinders of the same diameter at subcritical Reynolds number [24]. In this study, tandem cylinder flow is classified into regimes based on the ratio L/D where L is the center-to-center length between the cylinders and D is the cylinder diameter. Using the results of this study, Kozlov et al. examined the wake interaction of tandem cylinders in the intermittent shedding regime [17]. Both spanwise actuators and PSVGs were applied to the upstream cylinder, and were successful in reducing Cp_{rms} by 65% and 47%, respectively. This was accomplished by means of reducing the extent of large-scale vortex shedding in the upstream cylinder wake as shown in Figure 1.5. While the acoustic effects of this were not documented experimentally, simulations demonstrated the reduction of peak sound pressure level by approximately 16 dB, confirming the viability of plasma actuation for active aeroacoustic control of airframe noise [6].

1.4.3 Shock Strut-Torque Arm Assembly Plasma Flow Control

Studies performed by Neuhart et al., identified the torque arm as a region of high noise production on aircraft landing gear. Huang et al. studied the acoustic effects of plasma actuators on a torque arm apparatus [13]. By applying spanwise plasma actuators in both 'upstream' and 'downstream' configurations, two types of flow control were explored. The upstream configuration served to create a virtual plasma fairing effect by routing the shear layers around the downstream components, reducing the overall noise generated by wake impingement. The downstream configuration is shown to have reduced vortical structures, lowering the unsteadiness in the wake. The downstream and upstream configurations reduced far-field noise by 1.7 and 3.1 dB, respectively [13]. Wicks et al. also studied this geometry [22]. The spanwise actuation strategy was utilized and flow visualization is given in Figure 1.5.

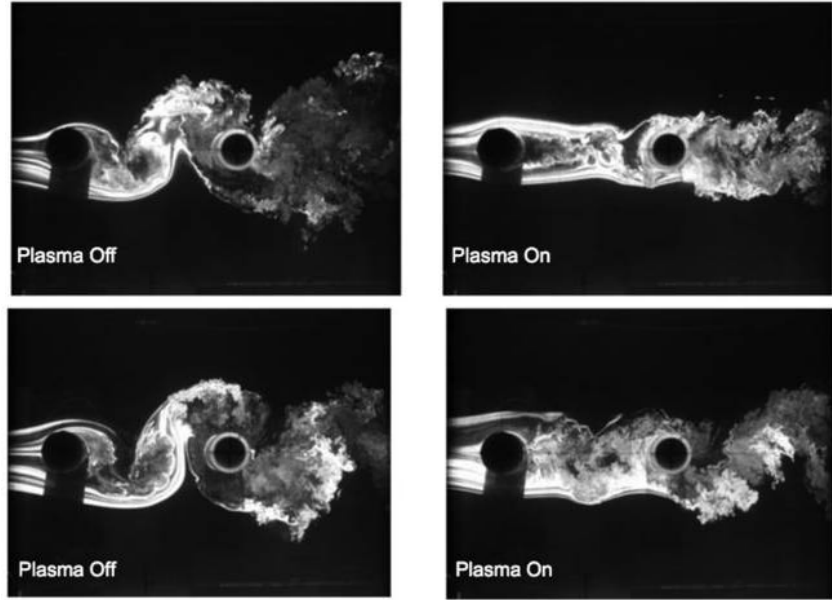


Figure 1.4. Flow Visualization of tandem cylinders in cross-flow with Spanwise and PSVG plasma actuators.

While this study did not focus on acoustic measurements, surface pressure spectra revealed a significant reduction in unsteady surface pressure associated with the wake of the upstream cylinder. Unfortunately, this had the adverse effect of increasing the energy of the wake of the downstream cylinder, demonstrating a fundamental difference between this geometry and the tandem cylinders. It also suggests perhaps a flow control strategy emphasizing the reduction of the extent of the wake impingement as opposed to large-scale vortex shedding may prove more successful in noise reduction.

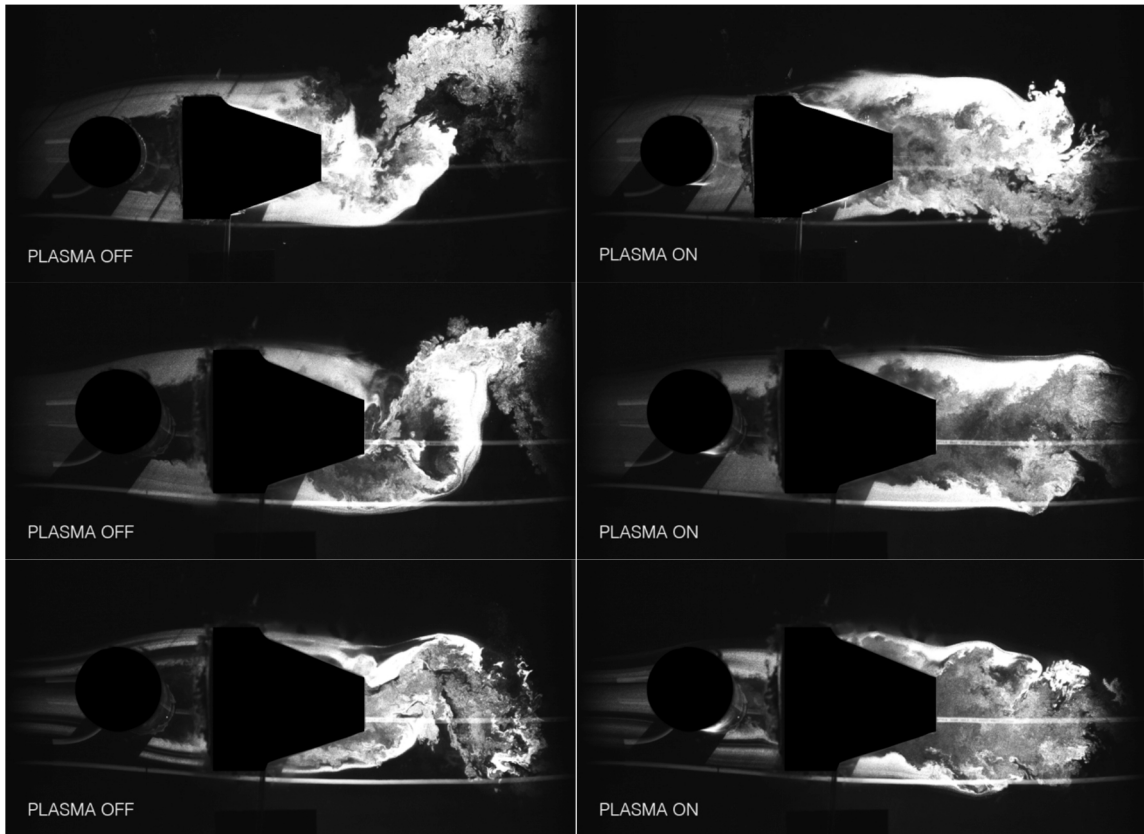


Figure 1.5. Flow Visualization of torque-arm assembly in cross-flow with Spanwise plasma actuators.

CHAPTER 2

EXPERIMENTAL APPROACH

The following chapter provides details on the experiments completed to date

2.1 Experimental Objective

Several key features of the flow over aircraft landing gear geometry have yet to be fully understood. One such feature is the main strut and door interaction. The preliminary experiments outlined in this chapter, exploring this interaction, have revealed potentially viable flow control strategies to be investigated in the proposed experiments outlined in chapter 3.

2.2 Experimental Facility

Acoustic measurements were obtained in the Notre Dame Anechoic Wind Tunnel Facility (ND AWT). The ND AWT is a low-noise, open-jet acoustic wind tunnel with a free jet test section measuring 24-in-(0.610 m)-high by 24-in-(0.610 m)-wide installed in a large anechoic chamber suitable for frequencies above 100 Hz. The maximum empty test section velocity is approximately $U_\infty = 35$ m/s. The maximum safe tunnel velocity with the Notre Dame G550 Nose Landing Gear 30%-scale model (ND G550) installed is 30 m/s corresponding to a Mach number of $M_\infty = 0.1$.

Atmospheric properties such as ambient temperature and pressure were acquired using a digital thermometer and barometer. The tunnel speed is measured using a pitot-static probe installed approximately 6 in (0.154 m) from the free jet inlet centerline. From these data local sonic speed and the flow Mach number are computed.



(a) Baseline 1



(b) Baseline 2

Figure 2.1. ND G550 model with and without plasma fairing installed.

2.3 Notre Dame G550 Nose Landing Gear Model

The Notre Dame G550 (ND G550) nose landing gear model has two baseline configurations without plasma actuation. The first, designated Baseline 1, consisted of the ND G550 model without the plasma fairing installed, which is shown in the photograph of Figure 2.1a. The second, designated Baseline 2, involved the ND G550 model retrofitted with a plasma fairing assembly in order to facilitate the installation of DBD plasma actuators for flow control. This configuration is shown in the photograph of Figure 2.1b.

Spanwise plasma actuators were fixed to the $\pm 90^\circ$ locations to ascertain the effects on the flow. The plasma actuator was constructed using 1/8 in ULTEM dielectric and 1 in exposed and covered copper electrodes. Also, it was operated using a sine wave carrier frequency of 1 kHz with 40 kV peak-to-peak voltage. With this configuration, the plasma actuators can be operated in both two-sided and one-sided modes.

2.4 Microphone Measurements

A polar array of omnidirectional microphones was used to acquire far field noise level spectra along the length of the AWT test section. It consists of a 1/2-in ACO Model 7046 electret microphone with companion 4012 preamplifier and PS9200 power supply. A schematic illustrating the array is shown in Figure 2.2. Additionally, the array configuration relative to the G550 model is shown in the photograph of Figure 2.3. The microphone is mounted using a microphone stand so as to protrude from an acoustically treated rail by approximately 13 in (0.330 m). The total range of acoustic source-to-microphone angle spanned by the polar array is approximately $30^\circ \leq \theta \leq 150^\circ$ as referenced from the upper torque arm of the model in the downstream flow direction. As shown in Figure 2.3, the polar array is situated along the length of the free jet test section and positioned at the same height as the upper torque arm of the

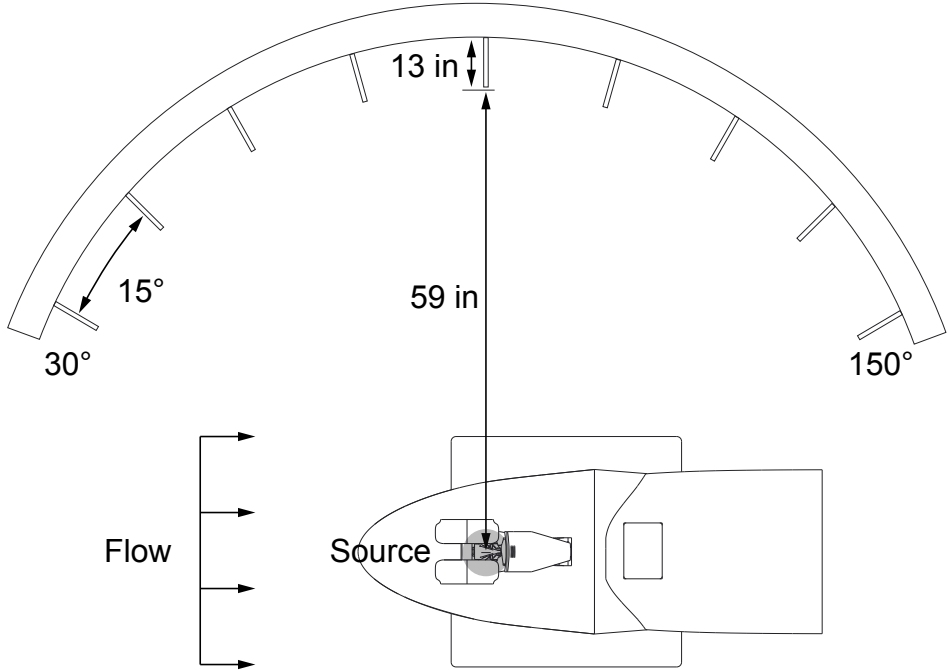


Figure 2.2. Schematic of the polar array.

model, with the plane of the microphone located approximately 59 in (1.50 m) from the test section centerline.

2.5 Flow Visualization

A commercial time-resolved PIV system comprising a Litron Nd:YLF ($\lambda = 527$ nm) dual-cavity laser and Photron SA1 high-speed camera (12 bit, maximum resolution 1280×800 pixels) was utilized. This system was operated in single-frame mode at a repetition rate of 2k frames per second (fps). Images were acquired with a spatial resolution of 1020×1020 pixels. During each run, $N = 2k$ images were recorded. A 60 mm Nikon Nikkor Micro lens was fitted and oriented orthogonal and 45° to the flow (to resolve region between main strut and door). The experimental setup is depicted in Figure 2.4.

Continuous DEHS fog consisting of nominally 1-mm-diameter droplets generated

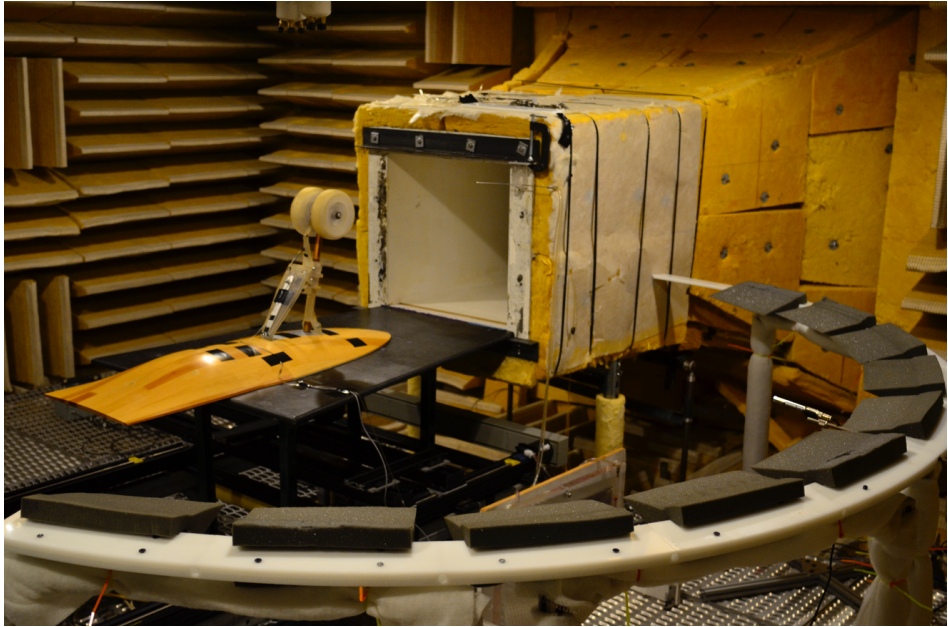


Figure 2.3. Photograph of the polar array installed in the ND AWT.

by a TSI six-jet particle atomizer were introduced upstream of the wind-tunnel inlet contraction. The Nd:YLF laser was used to illuminate the fog in a spanwise plane located 6 in from the base of the model. Flow visualization was performed with baseline 1, 2, and plasma on, in order to assess the global influence on the wake interaction with the main strut and door.

2.6 Data Acquisition

For microphone data acquisition, a National Instruments USB-6343 DAQ was used, yielding a total of 45 available channels with 48-bit ADC. The sampling parameters for the microphone data acquisition are listed in Table 2.1.



Figure 2.4. Photograph of the experimental setup for high speed flow visualization.

TABLE 2.1

Data acquisition parameters.

Sensors	Sampling Rate (Hz)	$\frac{Samples}{block}$	Window Function	Overlap (%)	N_{blocks}	$N_{averages}$	Acquisition Time (s)
ACO	65,536	2048	Hanning	0	960	960	30

2.7 Current Results

2.7.1 Wind Tunnel Background Noise Characterization

It was deemed important to establish that the background noise levels in the ND AWT were sufficiently below that of the ND G550 model. To that end, measurement of noise levels for both Baseline 1 and Baseline 2 G550 configurations were compared with those obtained with the AWT tunnel running empty. Figure 2.5 presents a representative comparison of 1/3-octave band sound pressure level (SPL) spectra obtained for the Baseline 1 configurations and the empty tunnel. The figure clearly shows that the background empty tunnel noise level is several orders of magnitude below that of the ND G550, so that the effects of plasma flow control on noise production will be detectable in this facility.

2.7.2 Far field check

This section describes a procedure for verifying the far field assumption for microphone measurements. For a microphone measurement to be classified as far field, the microphone-to-source distance must be greater than the acoustic wavelength. To check this, a relation can be made between power spectral density, PSD , and microphone-to-source distance, d . Recall from equation 1.9 that $p' \propto 1/d$, therefore, it follows that $PSD \propto 1/d$. Combining this relation at $d = 48$ in and $d = 59$ yields,

$$\frac{PSD_1}{PSD_2} \propto \frac{d_2}{d_1} \propto 1.23. \quad (2.1)$$

The $PSDs$ at both of these locations is plotted along with a reference line at 1.23 in Figure 2.6. The measured microphone data exhibits oscillations about the theoretical value of 1.23. Also, the average of the oscillations collapses to approximately this value if frequencies below 100 Hz are excluded. This suggests that to resolve frequencies below 100 Hz larger values for d are necessary. Previous experiments on

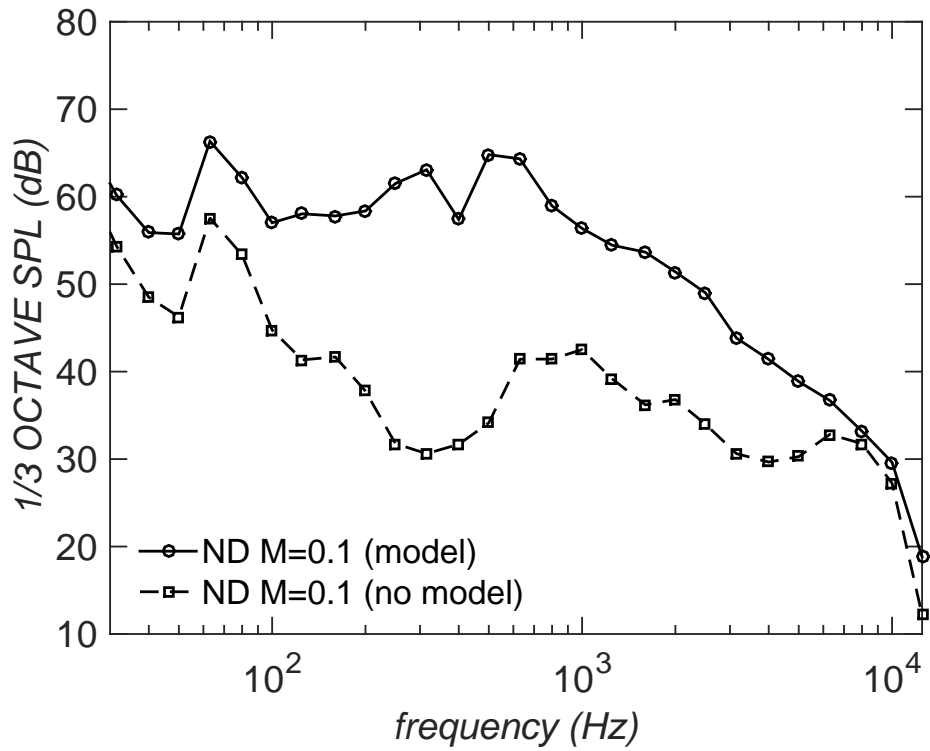


Figure 2.5. Representative far field noise level with and without Baseline 1 model installed at $\theta = 90^\circ$

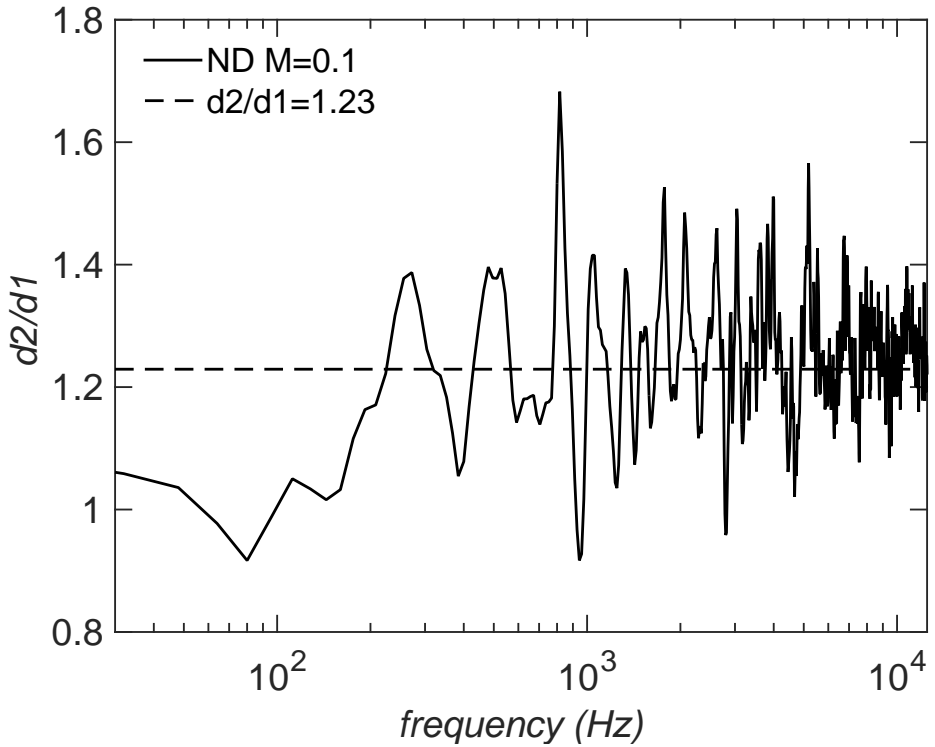


Figure 2.6. Far field measurement analysis for $d = 48$ in and $d = 59$ in at $\theta = 90^\circ$

landing gear geometry have reinforced that this lower limit on acoustic measurements is acceptable, as most observed flow behavior is attributed to frequencies above this cutoff.

2.7.3 Comparison with UFAFF Measurements

In this study, the far field microphone distance d , was 72 in (1.83 m) array-to-model and 59 in (1.50 m) microphone-to-model. However, previous studies conducted at the University of Florida Anechoic Flow Facility (UFAFF) on the NASA G550 model were performed at a source-to-microphone distance of 48 in. In order to form a basis for comparison with acoustic results from that study, 1/3-octave band SPL spectra were obtained with the ND Baseline 1 model in the ND AWT

for a source-to-microphone distance of 48 in (1.22 m). Even after accounting for the source-to-microphone distance disparity, the UFAFF experiments were performed at a freestream Mach number $M_\infty = 0.189$ and the Notre Dame experiments were performed at $M_\infty = 0.1$. The effect of disparate Mach numbers on the SPL can be accounted for by scaling the Notre Dame results via the relation,

$$SPL_2 = SPL_1 - 10 \log \left(\frac{M_1}{M_2} \right)^6, \quad (2.2)$$

where SPL_1 and M_1 denote the ND AWT experimental values, M_2 denotes the UFAFF test Mach number (0.189) and SPL_2 represents the ND AWT sound pressure level values corrected for Mach number. Figure 2.7 compares 1/3-octave band SPL spectra obtained in both facilities for the case of $\theta = 90^\circ$. In this plot the frequency is expressed in terms of Strouhal number, $St_D = fD/U_\infty$, where length scale D is the shock strut diameter upstream of the torque arm and U_∞ is the freestream velocity. There is good collapse of the NASA G550 and ND G550 data from $0.3 \leq St_D \leq 0.6$. Below this range there is about 4-5 dB difference before the 100 Hz AWT cutoff frequency. Above this range there is significant discrepancy. The NASA G550 model is characterized by a peak near $St_D = 3$ and spectral roll-off above this peak. The ND G550 model lacks this high frequency content. The components of the ND G550 model are mostly fabricated from SLA plastic, while the NASA G550 consists of mostly aluminum and carbon fiber. To compensate for the differences in tensile strength, thickness was added to several components of the ND G550 model as shown in the CAD images in Figure 2.8. Additionally, it was necessary to construct most of the ND G550 model from plastic to facilitate the retrofitting of plasma actuators. It is possible, but by no means certain that these design modifications may play a role in the observed differences in noise spectra.

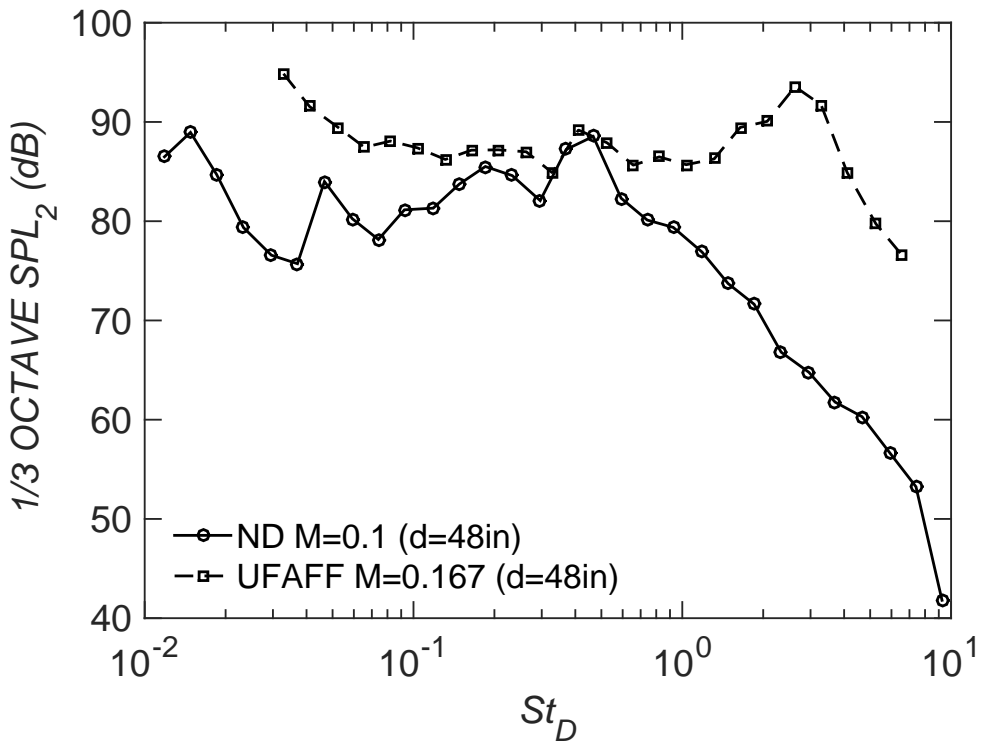


Figure 2.7. Comparison of far field noise level at UFAFF and ND AWT facilities at $\theta = 90^\circ$

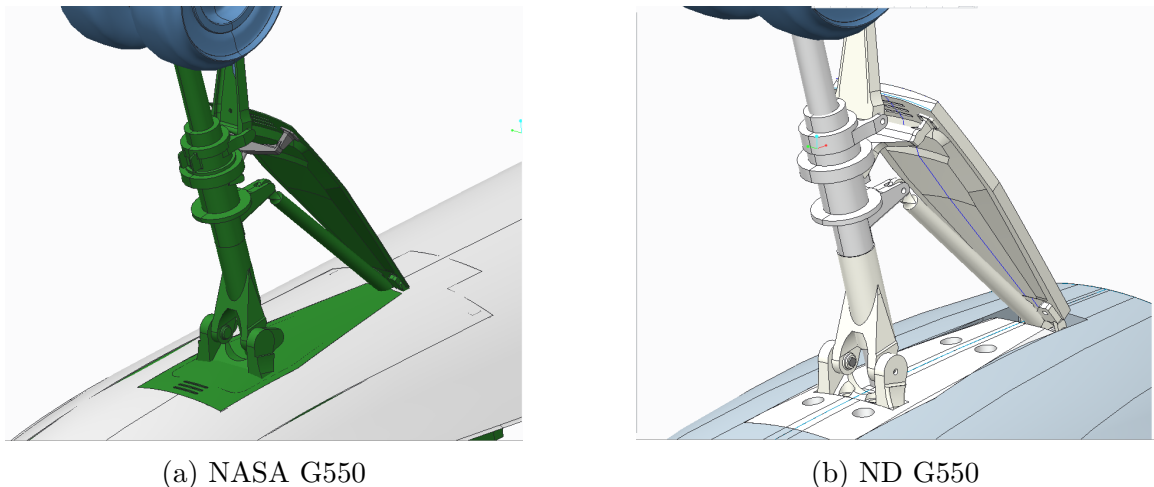


Figure 2.8. Comparison of design of the NASA G550 and ND G550 model geometries.

2.7.4 Effects of Tripping

Previous work on the NASA G550 Nose Landing Gear (NASA G550) involved application of serrated transition strips that were applied along the length of the shock strut in order to create a turbulent boundary layer prior to separation. For consistency with this previous work, the influence of similar aerodynamic trips was explored on the ND G550 Baseline 1 model. A distributed roughness element made of standard diving board tape was fixed to the shock strut. Sample results comparing 1/3-octave band SPL spectra for the tripped and untripped cases are presented in Figure 2.9. This figure shows that there was very little influence of the trip on radiated noise. Since a trip would restrict the optimum placement of the plasma actuators, it was omitted from the model and the acoustic results that follow were obtained without tripping unless otherwise indicated.

2.7.5 Preliminary Acoustic Assesment

Three key locations on the polar array were selected for microphone measurements. This allowed several plasma actuator configurations to be tested expediently to quickly assess noise reduction. Four plasma actuator configurations were utilized: 1) Baseline 1, 2) Baseline 2, 3) Sine 40 kV (Two-sides), 4) Sine 40 kV (One-side). The effect of the fairing geometry is shown with 1) and 2), while 3) and 4) demonstrate the effects of plasma actuation. The maximum peak-to-peak voltage attainable with the ULTEM dielectric was 40 kV before signs of dielectric failure were observed. In subsequent experiments, a dielectric that is less susceptible to failure, such as quartz, is recommended.

The 1/3-octave band SPL spectra for the aforementioned actuator configurations are given in Figure 2.10. Recall from Figure 2.5, that the left most peak is below the 100 Hz cutoff frequency and is most likely due to fan noise inherent to the facility. The acoustic signature at each location is characterized by two peaks at approximately

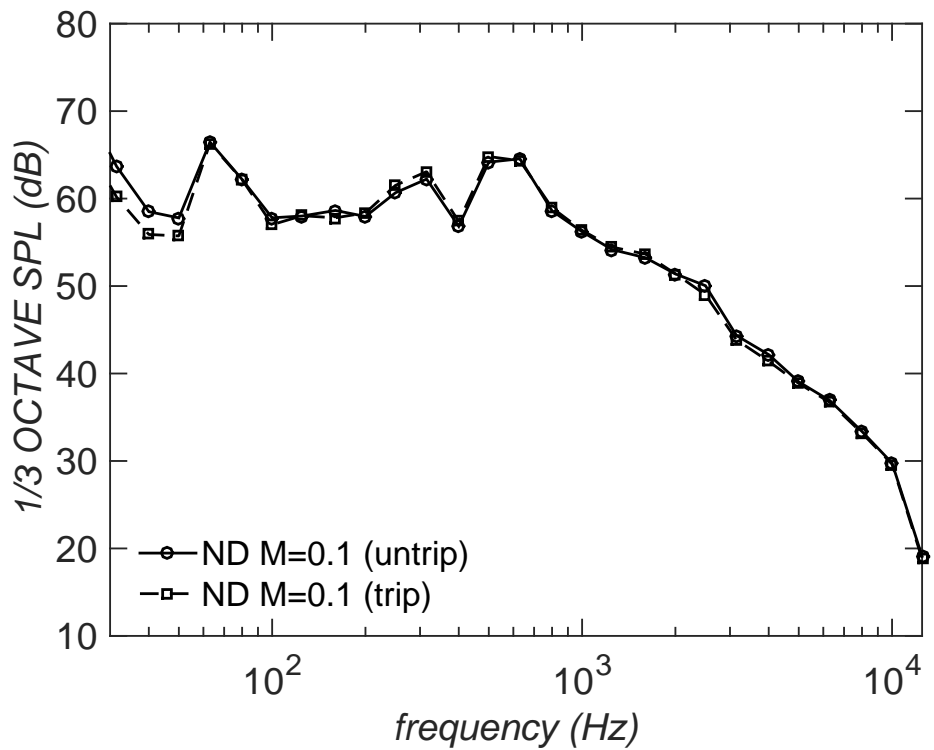


Figure 2.9. Comparison of far field noise level with and without the presence of a trip at $\theta = 90^\circ$

300 Hz and 500 Hz of varying magnitude. Most of the change caused by the plasma fairing occurs around these frequencies, with the exception of a slight increase in frequency due to the self-noise of the plasma actuators for $6 \leq f \leq 12.5$.

The Overall Sound Pressure Level (OASPL) is calculated by integrating the power spectral density from $100 \leq f \leq 1000$ Hz. This range was selected to eliminate any effects from the self-noise generated by the plasma actuator which is operated at a carrier frequency of 1000 Hz. OASPL at each location, $\theta = 45^\circ, 90^\circ, 135^\circ$, is given in Figure 2.11. There is a slight decrease for the Baseline 2 and sine 40 kV one-side cases at $\theta = 135^\circ$ of 0.12 dB and 0.13 dB, respectively. Also, the plasma actuation actually increased the noise at each location with the exception of the sine 40 kV one-sided case at $\theta = 135^\circ$.

To better understand the perplexing results of the acoustic measurements, flow visualization was performed to resolve the change to the global flow field and the effects on the main strut and door wake interaction. These images are given in Figure 2.12. When comparing the global flow field of Baseline 1 and 2, it is clear that the addition of the fairing acts to increase the spanwise extent of the wake caused by the upstream main strut. This results in reduction of the impingement of the detached shear layers on the downstream door. Interestingly, the activation of the plasma actuators in both two-sided and one-sided modes created a global flow field closer to that of the Baseline 1 case. Also, the plasma actuators increased unsteadiness in region between the the main strut and door, resulting in a significant increase in noise.

While these initial results show an increase in noise due to plasma actuation, there are implications for favorable flow control strategies. Configurations of plasma actuators that direct the detached shear layers around landing gear components may result in a significant reduction in noise. This could be accomplished by using spanwise plasma actuators to ‘trip’ the flow, causing premature flow separation on the

plasma fairing. Additionally, wake unsteadiness could be accomplished by utilizing PSVGs to promote mixing, thereby reducing large-scale vortices in size.

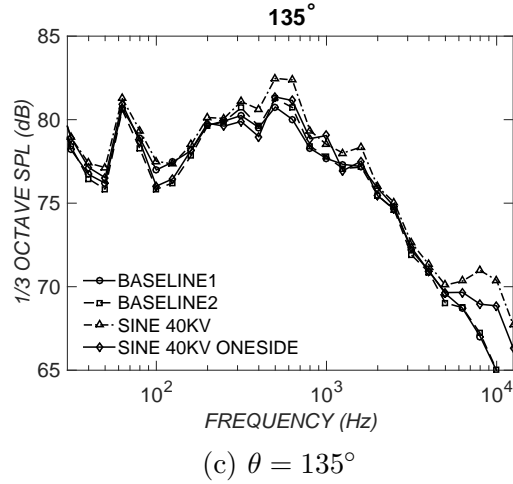
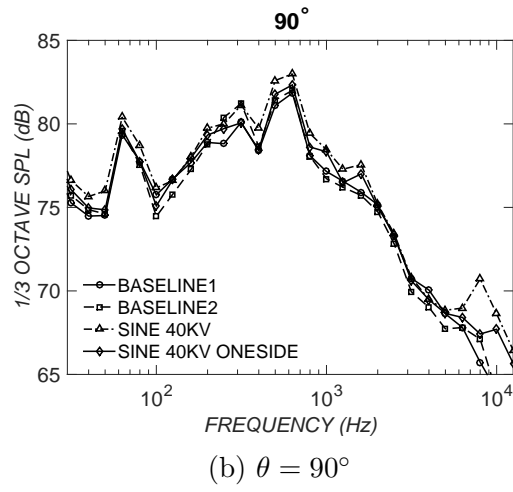
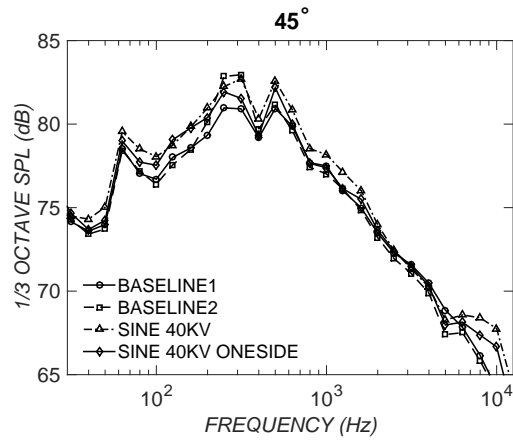


Figure 2.10. 1/3-octave band sound pressure level for various plasma actuator configurations.

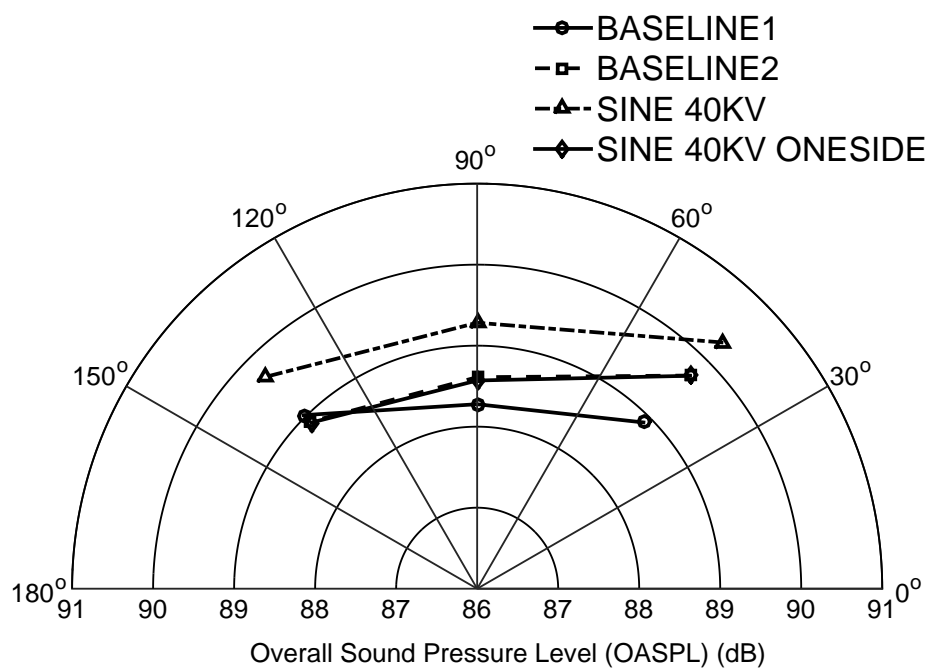


Figure 2.11. Overall sound pressure level at key polar array locations.



Figure 2.12. Landing gear flow visualization orthogonal (left) and at 45° (right).

CHAPTER 3

OBJECTIVES AND FUTURE WORK

This chapter outlines the research objectives and proposed future work.

3.1 Research Objectives

The overall focus of this study is the development of plasma fairing technology, however, much has yet to be accomplished before this technology is flight ready. To this end, the complex ND G550 geometry will be divided into two sub-systems: 1) main-strut-door assembly and 2) the shock-strut-torque-arm assembly. Flow control strategies will be explored for each of these subsystems varying plasma actuator configurations. Finally, the acoustic effects of the applied flow control will be characterized.

While the ultimate purpose of this research is the reduction of noise on aircraft landing gears, the objectives of this study will emphasize the documentation of the most successful flow control strategies and underlying physical mechanisms responsible. Regardless if noise reduction is actually achieved, there is much to be gained through a deeper understanding of the effects of various flow control strategies on noise generation.

3.2 Proposed Future Work

The following sections detail the experiments that will be performed to accomplish the outlined research objectives.

3.2.1 Plasma Actuator Configuration

Recall from Figure 2.1b, the plasma fairing that has been retrofitted to the ND G550 nose landing gear model. Plasma actuators will be fixed to this partial fairing geometry. Both spanwise and PSVG configurations will be explored. The effects of geometric parameters will be examined such as spanwise actuator azimuthal placement and upstream versus downstream forcing. Also, the effects of plasma actuation parameters such as voltage, frequency, and interelectrode spacing (PSVGs only).

As parameters are varied the changes to the flow field will be documented using high speed flow visualization similar to that in Figure 2.12. Particle Image Velocimetry (PIV) will be performed to quantify these flow fields and calculate the effects on vorticity, as changes to vorticity can result in significant changes to the acoustic signature.

From the preliminary results cited in the previous chapter, a minor reduction in noise was observed when the main strut wake impingement was reduced on the downstream door. Unsteady pressure sensors will be used at various locations near the door's edge to quantify the effect of varying the parameter space of the plasma actuator. Both power spectral density and RMS pressure coefficient will be calculated.

3.2.2 Noise Reduction Assessment

The plasma actuator configurations deemed most likely to reduce noise will be selected based on the previous measurements. These configurations will then be tested on the model in the AWT facility. The polar array depicted in Figure 2.3 will be used to measure magnitude and directivity of noise generated by baseline model and with plasma actuators installed. The difference in overall sound pressure level (OASPL) will also be calculated. It is possible that iteration will be necessary to identify the most promising plasma actuator configurations, as reduction in unsteady pressure is

not necessarily indicative of noise reduction of a similar magnitude. Finally, phased-array noise source identification will be performed to reveal where on the ND G550 model, flow control was most effective. Analysis of the underlying mechanisms will also be presented, by correlating aerodynamic and acoustic data.

3.3 Conclusion

While preliminary experiments demonstrate only a marginal effect of plasma flow control on noise reduction, flow visualization suggests a “path forward”, by focusing on the elimination of wake impingement of the main strut on the door. Additionally, studies performed on the shock strut and torque arm geometries confirm that this flow control strategy may apply to other locations of aircraft landing gear. Several plasma actuator configurations will be utilized while documenting both the aerodynamic and acoustic effects. This study will focus on the underlying physical mechanisms responsible for noise production on the ND G550 nose landing gear model and the effects of flow control via plasma actuation.

BIBLIOGRAPHY

1. M. A. Busquin. European aeronautics: A vision for 2020, meeting society's needs and winning global leadership. Rept. of the group of personalities, Advisory Council for Aeronautics Research in Europe, Jan 2001.
2. A. W. Correia, J. L. Peters, J. I. Levy, S. Melly, and F. Dominici. Residential exposure to aircraft noise and hospital admissions for cardiovascular diseases: multi-airport retrospective study. *BMJ*, 347, 2013.
3. N. Curle. The influence of solid boundaries upon aerodynamic sound. *Proceedings of the Royal Society A: Mathematical and Physical Sciences*, 231(1187):505–514, 1955.
4. W. Dobrzynski. Almost 40 years of airframe noise research: What did we achieve? *Journal of Aircraft*, 47(2):353–367, April 2010.
5. W. Dobrzynski, L. C. Chow, P. Guion, and D. Shiells. Research into landing gear airframe noise reduction. AIAA/Conference European Aerospace Societies Paper 2002-2409, June 2002.
6. A. Eltawee, M. Wang, D. Kim, F. O. Thomas, and A. Kozlov. Numerical investigation of tandem-cylinder noise reduction using plasma-based flow control. *J. Fluid Mech*, 756:422–451, 2014.
7. Environmental Research and Consultancy Department. Aircraft noise, sleep disturbance and health effects cap 1164. Technical report, June 2014.
8. J. S. Gibson. Non-engine aerodynamic noise investigation of a large aircraft. NASA CR-2377, 1974.
9. Gulfstream Aerospace Corporation. *G-550 Aircraft Maintenance Manual*. 2014.
10. Y. Guo, R. Stoker, and K. Yamamoto. Experimental study on aircraft landing gear noise. *Journal of Aircraft*, 43(2):306–317, 2009.
11. A. Hirschberg and S. W. Rienstra. *An introduction to aeroacoustics*. Eindhoven University of Technology, 2004.
12. M. S. Howe. *Theory of Vortex Sound - Lighthill's Theory*. Cambridge University Press, 2003.

13. X. Huang, X. Zhang, and Y. Li. Broadband flow-induced sound control using plasma actuators. *Journal of Sound and Vibration*, 329(13):2477–2489, 2010.
14. M. R. Khorrami, M. M. Choudhari, L. N. Jenkins, and C. B. McGinley. Unsteady flowfield around tandem cylinders as prototype for component interaction airframe noise. 11th AIAA/CEAS Aeroacoustics Conference AIAA Paper 2005-2866, 2005.
15. D. Kim and M. Wang. Large eddy simulations of flow over a circular cylinder with plasma based control. 47th AIAA Aerospace Sciences Meeting AIAA Paper 2009-1080, 2009.
16. A. V. Kozlov and F. O. Thomas. Bluff-body flow control via two types of dielectric barrier discharge plasma actuation. *AIAA Journal*, 49(9):1919–1931, 2011.
17. A. V. Kozlov and F. O. Thomas. Plasma flow control of cylinders in a tandem configuration. *AIAA Journal*, 49(10):2183–2193, 2011.
18. M. J. Lighthill. On sound generated aerodynamically. ii. turbulence as a source of sound. *Proceedings of the Royal Society A: Mathematical and Physical Sciences*, 222(1148):1–32, 1954.
19. D. H. Neuhart, M. R. Khorrami, and M. M. Choudhari. Aerodynamics of a gulfstream g550 nose landing gear model. 15th AIAA/CEAS Aeroacoustics Conference AIAA Paper 2009-3152, 2009.
20. H. J. Price. Faa forecast sees continued, steady growth in air travel. Website, 2015. <http://www.faa.gov>.
21. P. A. Ravetta, R. A. Burdisso, and W. F. Ng. Noise control of landing gears using elastic membrane-based fairings. AIAA/Conference European Aerospace Societies Paper 2007-3466, May 2007.
22. M. Wicks, F. O. Thomas, T. C. Corke, C. Nelson, M. Patel, and A. B. Cain. Plasma flow control on a landing gear model. 53rd AIAA Aerospace Sciences Meeting AIAA Paper 2015-1036, 2015.
23. N. S. Zawodny, F. Liu, T. Yardibi, L. Cattafesta, D. H. Neuhart, and T. Van de Ven. A comparative study of a 1/4-scale gulfstream aircraft nose gear model. 15th AIAA/CEAS Aeroacoustics Conference AIAA Paper 2009-3153, 2009.
24. M. M. Zdravkovich. Flow induced oscillations of two interfering circular cylinders. *Journal of Sound and Vibration*, 101(4):511–521, 1985.

This document was prepared & typeset with pdfL^AT_EX, and formatted with NDDiss2_E classfile (v3.2013[2013/04/16]) provided by Sameer Vijay and updated by Megan Patnott.